

How Should Microrobots Swim?

Jake J. Abbott, Kathrin E. Peyer, Lixin Dong, and Bradley J. Nelson

Institute of Robotics and Intelligent Systems, ETH Zurich
8092 Zurich, Switzerland bnelson@ethz.ch

Summary. Microrobots have the potential to dramatically change many aspects of medicine by navigating bodily fluids to perform targeted diagnosis and therapy. Researchers have proposed numerous microrobotic swimming methods, with the vast majority utilizing magnetic fields to wirelessly power and control the microrobot. In this paper, we theoretically and experimentally compare the two most promising methods of microrobot swimming—using magnetic fields to rotate helical propellers that mimic bacterial flagella, and pulling with magnetic field gradients—considering the practical limitations in the generation of magnetic fields. We find that swimming with a helical propeller generally becomes more desirable as size decreases, and will likely be the best choice for *in vivo* applications.

1 Introduction

Microrobots have the potential to dramatically change many aspects of medicine by navigating bodily fluids to perform targeted diagnosis and therapy. Microrobots, like microorganisms, swim in a low-Reynolds-number regime, requiring swimming methods that differ from macroscale swimmers [1]. However, microrobots can also vary in size by orders of magnitude. Researchers have proposed numerous microrobotic swimming methods, many biomimetic, with the vast majority utilizing magnetic fields to wirelessly power and control the microrobot. It remains unclear which propulsion method is optimal, and a comparison that considers the microrobot's size coupled with the practical limitations in generating magnetic fields is needed. To do this we have developed two different magnetic microrobots that utilize very different propulsion schemes: one is a submillimeter-sized device that is pulled with magnetic field gradients (Figure 1(a)); the other has a helical propeller that mimics a bacterial flagellum in both form and scale and is rotated with a magnetic field (Figure 1(b)). In this paper, we compare these two propulsion methods, which are representative of the majority of active research in wireless microrobots. We show that metrics of efficiency, which are often used to characterize low-Reynolds-number swimming, can be quite misleading, and that practical

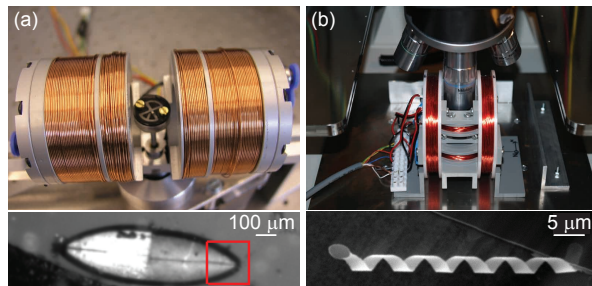


Fig. 1. Swimming microrobots with a 30:1 size difference. Magnetic fields (a) pull a 900- μm assembled-MEMS Ni microrobot [2], and (b) rotate a 30- μm microrobot with a helical-nanocoil “flagellum” with a Ni “head” [3].

limitations in magnetic control greatly impacts which method is best for a given application. We show that swimming with a helical propeller generally becomes more desirable as size decreases and will likely be the best choice for *in vivo* applications. We also find that limitations in the hardware used to generate the magnetic fields can influence which swimming method is best.

2 Swimming at Low Reynolds Number

It has long been known that swimming at the microscale requires techniques that are very different from those used by macroscale swimmers such as fish and humans [1]. To understand this phenomenon, we turn to the Navier-Stokes equations, which, when combined with boundary conditions, completely define a fluid flow. For a fluid with constant density ρ and constant viscosity η , the Navier-Stokes equations are given by a single vector equation, which can be nondimensionalized in space and time by the magnitude of the free-stream velocity \mathcal{V} and some characteristic length \mathcal{L} :

$$\left(\frac{\rho\mathcal{V}\mathcal{L}}{\eta}\right)\frac{d\mathbf{V}}{dt} = -\nabla p + \nabla^2\mathbf{V} \implies Re = \frac{\rho\mathcal{V}\mathcal{L}}{\eta} \quad (1)$$

\mathbf{V} is the velocity vector field and p is the hydrodynamic pressure scalar field, which have both been nondimensionalized as detailed in [4]. From this equation we discover the Reynolds number, the dimensionless quantity that embodies the interaction between a fluid’s inertia and viscosity. At low Re , we are in a world that is either very viscous, very slow, or very small. Low- Re flow around a body is referred to as creeping flow or Stokes’ flow. We no longer see a transition to turbulence, even behind bluff bodies. At low Re , the role of time becomes negligible in (1); the flow pattern does not change appreciably whether it is slow or fast, and the flow is reversible. Consequently, reciprocal motion (i.e., body motion that simply goes back and forth between two configurations) results in negligible net movement.

Microorganisms are able to swim at low Re using a variety of techniques [5], none of which look like macroscale swimmers (Figure 2). Cilia are active organelles that are held perpendicular to the flow during the power stroke and

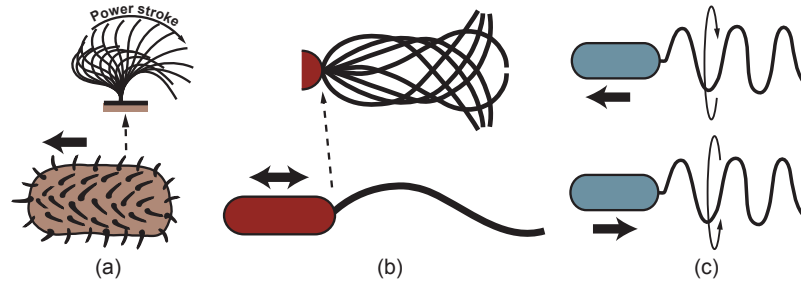


Fig. 2. Locomotion of microorganisms, adapted from [6]. (a) Cilia move across the flow during the power stroke, and fold near the body during the recovery stroke. (b) Eukaryotic flagella create patterns such as propagating waves or circular translating movements. (c) Molecular motors spin bacterial flagella, which act somewhat like corkscrews.

parallel to the flow during the recovery stroke. Many cilia are used simultaneously. Eukaryotic flagella are active organelles that deform to create paddling motions, such as propagating waves or circular translating movements. Bacterial (prokaryotic) flagella work differently by using a molecular motor to turn the base of the flagellum, which acts somewhat like a corkscrew. Some bacteria have multiple flagella that bundle during swimming. All of the swimming methods utilized by microorganisms are fairly inefficient, which is not a problem because microorganisms' source of energy (food) is so plentiful.

A number of robotic swimming methods have been shown to work at relatively small scales, but will have reduced effectiveness as size decreases to the microscale because they make use of reciprocating configurations. Other biomimetic swimming methods utilize physics that scale well to the microscale. Artificial eukaryotic flagella use distributed actuation to create a propagating wave [7]. The need for distributed actuation can be somewhat overcome using a reciprocating magnetic field to generate propagating-wave-like motion in a flagellum [8]. There is a great deal of interest in microrobot swimming using helical propellers that mimic bacterial flagella. Helical propellers can be made rigid, removing the need for distributed actuation, and it is now possible to fabricate these structures at the microscale [9]. Alternatively, it has been suggested that the microrobot's payload, such as a strip of drug, can be twisted up into a helical propeller to actually contribute to propulsion [10]. Other screw-like robots have made use of helical propulsion as well [11].

A controllable external pulling source is not available to microorganisms, but engineers can utilize gradients in magnetic fields to apply forces and torques to untethered microrobots [2, 12]. This greatly simplifies fabrication since no microactuator or special structure is needed for propulsion. It is also reasonable to wonder if this form of propulsion, which could not have evolved through natural selection, might outperform biomimetic methods.

3 Magnetic Power and Control

Nearly every demonstrated and proposed method for wireless power and control of microrobots utilizes magnetic fields. No other actuation principle offers the ability to transfer such large amounts of power wirelessly. In addition to pulling with field gradients, a rotating magnetic field is an obvious choice to rotate a helical propeller [3, 13], eliminating the need to replicate a molecular motor in a microrobot. However, even with all of their positive attributes, magnetic fields impose strict limitations on the design of wireless microrobots.

If we want to apply controlled forces and torques to a body with magnetization \mathbf{M} using a controlled magnetic field \mathbf{H} (both quantities are vectors with units A/m), the governing control equations are as follows [14]. The magnetic torque tends to align the magnetization of the body with the applied field:

$$\mathbf{T} = \mu_0 v \mathbf{M} \times \mathbf{H} \quad (2)$$

where v is the volume of the body in m^3 and $\mu_0 = 4\pi \times 10^{-7} \text{ T}\cdot\text{m}/\text{A}$ is the permeability of free space. The magnetic force on the body is

$$\mathbf{F} = \mu_0 v (\mathbf{M} \cdot \nabla) \mathbf{H} \quad (3)$$

We can also express the applied magnetic field as an applied magnetic flux density \mathbf{B} with units T. \mathbf{B} is related to \mathbf{H} simply as $\mathbf{B} = \mu_0 \mathbf{H}$.

If the body of interest is a permanent magnet, the magnetization \mathbf{M} is effectively constant with respect to the body with a magnitude equal to the remanence magnetization of the material. We can increase torque by increasing the angle between \mathbf{H} and \mathbf{M} , up to 90° , or by increasing the strength of \mathbf{H} . We can increase force by increasing the gradients in the applied field. If the body of interest is made of a soft-magnetic material, the magnetization is a nonlinear function of the applied field and can rotate with respect to the body; the governing equations for control are significantly more complex [4].

Controlled magnetic fields can be generated with electromagnets that are position and current controlled [2], by orthogonal stationary current-controlled electromagnets [15], by position-controlled permanent magnets such as with Stereotaxis' Magnetic Navigation System, or even by a commercial MRI system [12]. However, the rapid decay of magnetic field strength with distance \mathcal{D} from its source creates a major challenge for magnetic control. In practice, the geometry of a field source is important near the source, but we generally observe that the strength of a magnetic field decreases as $\sim \mathcal{D}^{-3}$. In addition, we find that the gradients in the field decay even faster, as $\sim \mathcal{D}^{-4}$.

4 Swimming with a Helical Propeller

An alternative to generating propulsive forces using magnetic field gradients is to use a helical propeller with parameters defined as shown in Figure 3. We

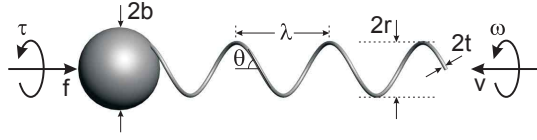


Fig. 3. Definition of parameters for a helical propeller. The force f and torque τ are those not due to the fluid.

follow a similar derivation to [16], a difference being that [16] assumes that the body slowly rotates counter to the helix to balance angular momentum (as a bacterium would due to flagellar rotation at a molecular motor), while we assume the helix is rigidly connected to the body. The result is a propulsion matrix relating the four principle quantities—forward velocity v , angular velocity ω , applied torque τ , and applied load f —for our helical swimmer:

$$\begin{bmatrix} f \\ \tau \end{bmatrix} = \begin{bmatrix} -2\pi nr (C_l c^2 + C_n s^2) / s - D_v & 2\pi nr^2 (C_n - C_l) c \\ 2\pi nr^2 (C_l - C_n) c & 2\pi nr^3 (C_n c^2 + C_l s^2) / s + D_\omega \end{bmatrix} \begin{bmatrix} v \\ \omega \end{bmatrix} \quad (4)$$

where $s = \sin \theta$ and $c = \cos \theta$, n is the number of turns of the helix (such that the helix length is $n\lambda$), and D_v and D_ω are linear and angular drag coefficients for the body, respectively. The constants C_n and C_l are the viscous drag coefficients for a thin cylindrical element of the propeller for flow normal to the cylinder’s axis and along the length of the cylinder’s axis, respectively:

$$C_n = \frac{4\pi\eta}{\ln\left(\frac{0.36\pi r}{t \sin \theta}\right) + \frac{1}{2}} \quad , \quad C_l = \frac{2\pi\eta}{\ln\left(\frac{0.36\pi r}{t \sin \theta}\right)} \quad (5)$$

where η is the fluid’s viscosity [17]. If we consider a spherical body, the drag coefficients are described simply in Stokes’ flow:

$$D_v = 6\pi\eta b \quad , \quad D_\omega = 8\pi\eta b^3 \quad (6)$$

A motivating factor for the use of helical propulsion is that we can now microfabricate nanocoils by rolling up prestressed bilayers [9]. This technique has better control over helical geometry than grown helical carbon nanotubes or ZnO nanobelts. The radius of the coil is determined by the Young’s moduli of the materials and the lattice mismatches of the bilayers. The geometrical relation of the nanocoil parameters is shown in Figure 4(a). The width of the stripe is given by its initial pattern design, and the depth is controlled during fabrication. Figure 4(b) shows the process sequence to fabricate nanocoil microrobots, which consist of a 27-nm-thick ribbon that, upon wet etch release, self-forms into a 3 μm -diameter coil with a length between 30 and 40 μm . A 2 $\mu\text{m} \times 2 \mu\text{m} \times 0.2 \mu\text{m}$ Ni plate is formed on one end that serves as a “head” [3]. Figure 4(c) shows an SEM image of an as-fabricated nanocoil with a Ni plate on one end. For the first propulsion experiment, individual magnetic nanocoils were immersed in paraffin oil, actuated with a rotating magnetic field (Figure 1(b)), and their motion was captured on video through a microscope [3]. One sequence for a 30- μm -long nanocoil is shown in Figure 4(d). The time for one rotation is 0.39 s. An axial velocity of 3.9 $\mu\text{m}/\text{s}$ is estimated from the figure.

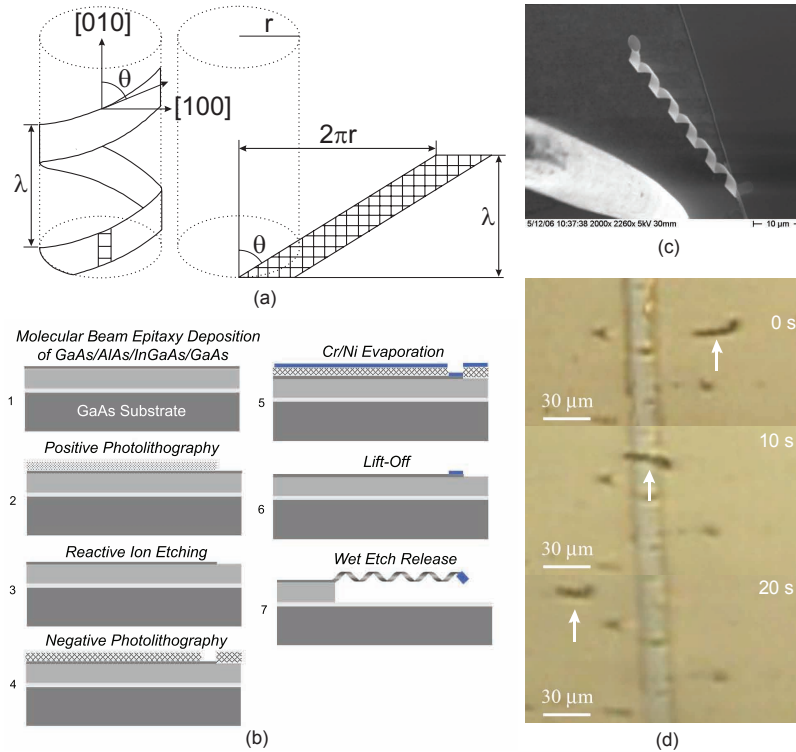


Fig. 4. Nanocoils as artificial bacterial flagella. (a) Schematic drawing showing the relationship between the stripe and etching direction in nanocoil parameters. Image courtesy of Li Zhang, ETH Zurich [9]. (b) Process sequence: initial planar, epitaxial bilayer with Ni parts, all patterned through conventional microfabrication techniques, self-forms into a 3-D nanostructure during wet etch release. (c) SEM image of an as-fabricated nanocoil with a Ni plate attached to one end. The probe tip that is used to break the attachment of individual coils is also visible. (d) A 30- μm nanocoil rotated in oil with a magnetic field, which results in forward motion [3].

5 Pulling versus Helical Propulsion

In order to make a fair comparison between microrobots that utilize rotating magnetic fields and a helical propeller and microrobots that are pulled by magnetic field gradients, we must consider the hardware that generates the magnetic field. In practice, there will be limits to how close the field sources can be placed to the microrobot. Let us compare the control of a microrobot with two current-carrying coils, as shown in Figure 5. Our field sources are assumed to be located a distance L from our microrobot. The limitations imposed by this two-coil system are representative of other magnetic control systems, such as those as described in Section 3. We will assume a simple magnetic bead of radius b for our microrobot. We have two options for control:

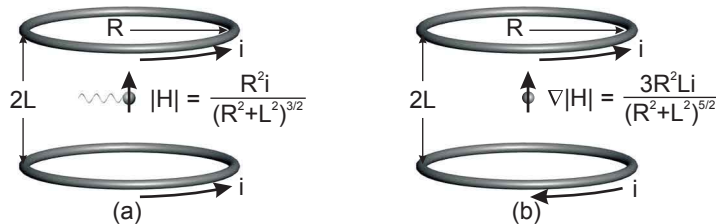


Fig. 5. (a) Uniform magnetic fields are generated by two coils with the current flowing in the same direction. The field can be used to rotate a microrobot. The field is calculated accurately with a current-loop model [14]. (b) Gradient fields can be generated by the same hardware by running the current in opposite directions. The gradient can be used to pull on a microrobot.

we can attach a helical propeller to our bead and then apply current in the same direction in the two loops, creating a uniform field that is used to rotate and thus propel the bead; or, we can apply the current in opposite directions, creating a field gradient that is used to pull on the bead directly. From the equations that describe the magnetic field and field gradient at the midpoint of the current loops [14], shown in Figure 5, we see that the field that we can generate changes with the gap between the two loops as $\sim L^{-3}$, while the gradient that we can generate changes as $\sim L^{-4}$, as expected. We also find that there are optimal values for the coil radii for a given coil gap to maximize the respective quantities: $R = \sqrt{2}L$ for case (a) and $R = \sqrt{2/3}L$ for case (b).

In Figure 6 we plot the maximum no-load ($f = 0$) velocity and the maximum stall ($v = 0$) force versus bead size. For the helical parameters, we choose $r = b$, $t = 0.01b$, and $\theta = 45^\circ$. Under present-day limitations in nanocoil fabrication, these parameters can be achieved for a bead size as low as $b = 1 \mu\text{m}$. For the coil gap, we assume $L = 0.2 \text{ m}$, which is the approximate value that would be needed to control a microrobot somewhere inside a human head. To avoid biasing the results, we use the optimal radii R for the respective cases. The results for two helices are shown: one for $n = 3$, and one for $n = 10$. The magnetization of the bead and the current through the loops enter into the maximum velocity and force linearly, so we can normalize our results to these quantities. The reciprocal of viscosity enters into the maximum velocity linearly, so we can normalize to this quantity as well; the viscosity has no bearing on the maximum force, even for the helical propeller.

We find that the maximum velocity varies as $\sim b$ for helical propulsion and as $\sim b^2$ for pulling. We find that the maximum force varies as $\sim b^2$ for helical propulsion and as $\sim b^3$ for pulling. This indicates that there will always exist a microrobot size below which using helical propulsion is desirable over pulling with field gradients. In addition, even though the helical parameters used were not optimized, Figure 6 indicates that helical propulsion is desirable over pulling for any microrobot size that would reasonably be considered as microscale.

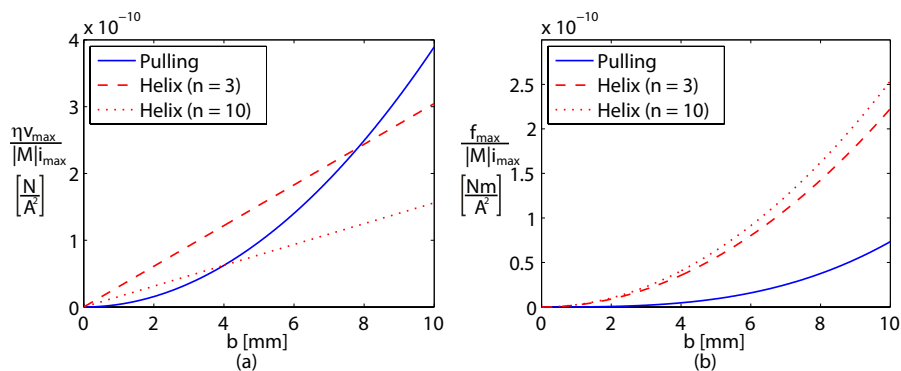


Fig. 6. Comparison of (a) normalized no-load ($f = 0$) velocity and (b) normalized stall ($v = 0$) load vs. bead radius for helical propulsion and field-gradient pulling.

Although helical propulsion of a body is described as being quite inefficient compared with simply pulling the body through the fluid [1], this is misleading in the context of magnetic control. Theoretically, helical propulsion is likely to outperform pulling with field gradients by a large margin in the size range of microrobots. In addition, increasing the distance between the magnetic field sources and the microrobot (e.g. L), which will likely be necessary for *in vivo* applications, will always tend to improve helical propulsion relative to pulling, although the effectiveness of both will be reduced.

The linearity of helical propulsion in Stokes' flow, predicted in (4), has been experimentally verified many times [13, 16]. However, the actual propulsion-matrix values in (4) are subject to modeling errors. The model in (4) assumes that the body and the helical propeller do not affect each others' flow fields, which clearly cannot be true. In addition, the individual Stokes'-flow models are derived assuming an infinite extent of fluid. Figure 7 shows magnetic and hydrodynamic data for three steel beads, taken with a custom measurement system [18]. We see that the magnetic models are quite accurate, but the viscous drag coefficient D_v for Stokes' flow around a sphere is less accurate, due to the wall effects of the container. Wall effects have also been observed to affect the helical-propulsion model [16], and are generally important at low Reynolds number [5]. Helical-propulsion models also typically assume a perfectly rigid helix. In Figure 5 we show experimental data for a nanocoil still attached to the chip, like that seen in Figure 4(c), subjected to a magnetic field and characterized as a spring in [3]; the nanocoil is clearly not rigid. The characterization of the stiffness of artificial flagella [19] can be used for improved helical-propulsion models.

Theoretical models of microrobot swimming should be improved, but the discrepancy between the models at the microscale observed in Figure 6 might be too large to be drastically affected by improved models. However, there is another practical limitation in the magnetic control of helical swimmers that

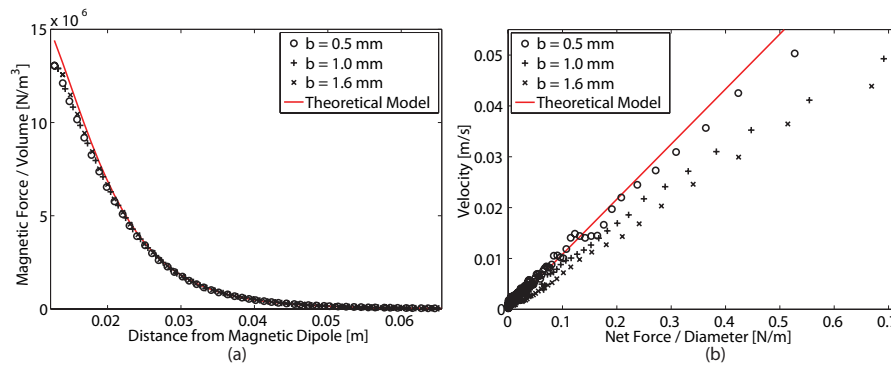


Fig. 7. Experimental results for three steel beads using a custom measurement system [18]. (a) Magnetic forces are accurately predicted using a theoretical model. (b) Hydrodynamic predictions of the beads being pulled through silicon oil ($\rho = 970 \text{ kg/m}^3$, $\eta = 0.98 \text{ Pa}\cdot\text{s}$) are less accurate, as Stokes' flow equations do not accurately account for wall effects of the 26-mm-diameter container.

we must consider. Our actual control variable is the rotation frequency ω of the magnetic field. The microrobot rotates in sync with the field, with the field leading the magnetization such that the magnetic torque from (2) balances the viscous torque. As ω is increased, the magnetic torque eventually reaches its maximum; this is the step-out frequency [11], above which the microrobot can no longer track the rotating field. The maximum velocity and force curves of Figure 6 assume that the microrobot is turning at its step-out frequency, which also increases linearly with the quantity $|\mathbf{M}|i/\eta$. For any field generation

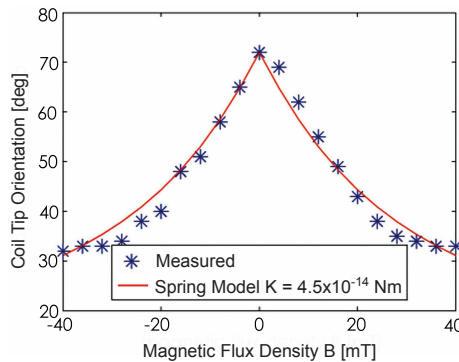


Fig. 8. A nanocoil attached to the chip, as shown in Figure 4(c), is subjected to a magnetic torque and characterized as a spring [3].

system, there are practical saturation limits in generating high ω due to, for example, motor speeds, induction, eddy currents, or sampling rates. If this ω -saturation is reached, the values shown in Figure 6 will over-estimate the capabilities of helical propulsion. We must also recall that the propulsion model implicitly assumes low- Re flow, which could be violated for very high ω . Thus, although it is always desirable to increase $|\mathbf{M}|$ and i for improved control using either swimming method, it could reduce the performance of helical propulsion relative to pulling.

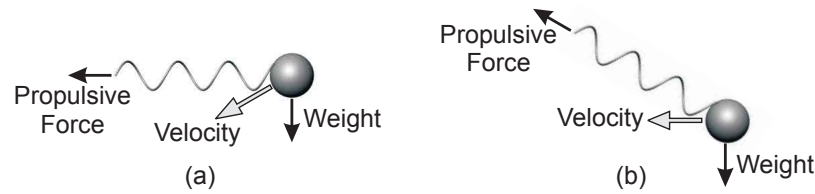


Fig. 9. (a) Simple helical propulsion results in drift due to gravity. (b) Swimming similar to helicopter flight can counteract gravity.

There is another factor that must be considered in microrobot swimming: gravity. It is often claimed that inertia is negligible at low- Re , but “inertia” is used differently here than “mass.” A microrobot will reach its terminal velocity in a fluid nearly instantaneously, and the terminal velocity decreases with size. However, even at low- Re , a microrobot will still fall downward under its own weight. The helical propulsion model developed in Section 4 assumes that flow is along the axis of the propeller. However, this only provides for propulsion along the axis, which will be insufficient to counteract gravity when swimming horizontally, as shown in Figure 9(a). It may be necessary to swim with an angle of attack, as shown in Figure 9(b), similar to the way a helicopter flies. Microorganisms that swim using flagella have a density similar to water, and are thus neutrally buoyant, making this effect of gravity on helical propulsion unique to microrobots that are constructed of denser-than-water materials.

Finally, it is possible to combine the benefits of field gradients with those of helical propulsion. That is, we can pull as we rotate. This hybrid method has the potential for improved performance. However, it will require a more complicated actuation scheme than that considered in Figure 5(a), and will likely place additional demands on localization needed for closed-loop control.

6 Conclusions

Magnetic fields provide an unequalled means of wireless power and control for microrobots. However, the strength of magnetic fields and field gradients decrease rapidly with distance from the source, which has a profound impact on the best way to make use of these fields for microrobot propulsion. Although it has been previously observed that a swimming microrobot with a helical propeller is far less efficient than simply pulling the microrobot through the fluid, we find that a helical propeller is theoretically far superior to pulling if we consider the limitations of magnetic field sources. We find that a helical propeller generally becomes preferable to pulling with field gradients as microrobot size decreases or as the distance from the magnetic field sources increases. Consequently, helical propulsion will likely be the best choice for *in vivo* applications. However, the design of hardware that realizes the theoretical possibilities of helical propulsion remains a challenging problem.

References

1. E. M. Purcell. Life at low Reynolds number. *American J. Physics*, 45(1):3–11, 1977.
2. K. B. Yesin, K. Vollmers, and B. J. Nelson. Modeling and control of untethered biomicrobots in a fluidic environment using electromagnetic fields. *Int. J. Robotics Research*, 25(5–6):527–536, 2006.
3. D. J. Bell, S. Leutenegger, K. M. Hammar, L. X. Dong, and B. J. Nelson. Flagella-like propulsion for microrobots using a magnetic nanocoil and rotating electromagnetic field. In *Proc. IEEE Int. Conf. Robotics and Automation*, pages 1128–1133, 2007.
4. J. J. Abbott, O. Ergeneman, M. P. Kummer, A. M. Hirt, and B. J. Nelson. Modeling magnetic torque and force for controlled manipulation of soft-magnetic bodies. *IEEE Trans. Robotics*, Accepted for Publication.
5. S. Vogel. *Comparative Biomechanics: Life's Physical World*. Princeton University Press, 2003.
6. J. J. Abbott, Z. Nagy, F. Beyeler, and B. J. Nelson. Robotics in the small, part I: Microrobotics. *IEEE Robotics and Automation Magazine*, 14(2):92–103, 2007.
7. G. Kósa, M. Shoham, and M. Zaaroor. Propulsion method for swimming microrobots. *IEEE Trans. Robotics*, 23(1):137–150, 2007.
8. R. Dreyfus, J. Baudry, M. L. Roper, M. Fermigier, H. A. Stone, and J. Bibette. Microscopic artificial swimmers. *Nature*, 437(6):862–865, 2005.
9. L. Zhang, E. Deckhardt, A. Weber, C. Schönenberger, and D. Grützmacher. Controllable fabrication of SiGe/Si and SiGe/Si/Cr helical nanobelts. *Nanotechnology*, 16:655–663, 2005.
10. H. Li, J. Tan, and M. Zhang. Dynamics modeling and analysis of a swimming microrobot for controlled drug delivery. In *Proc. IEEE Int. Conf. Robotics and Automation*, pages 1768–1773, 2006.
11. M. Sendoh, K. Ishiyama, and K. I. Arai. Direction and individual control of magnetic micromachine. *IEEE Trans. Magnetics*, 38(5):3356–3358, 2002.
12. J.-B. Mathieu, G. Beaudoin, and S. Martel. Method of propulsion of a ferromagnetic core in the cardiovascular system through magnetic gradients generated by an MRI system. *IEEE Trans. Biomedical Engineering*, 53(2):292–299, 2006.
13. T. Honda, K. I. Arai, and K. Ishiyama. Micro swimming mechanisms propelled by external magnetic fields. *IEEE Trans. Magnetics*, 32(5):5085–5087, 1996.
14. D. Jiles. *Introduction to Magnetism and Magnetic Materials*. Chapman and Hall, London, 1991.
15. D. C. Meeker, E. H. Maslen, R. C. Ritter, and F. M. Creighton. Optimal realization of arbitrary forces in a magnetic stereotaxis system. *IEEE Trans. Magnetics*, 32(2):320–328, 1996.
16. B. Behkem and M. Sitti. Design methodology for biomimetic propulsion of miniature swimming robots. *ASME J. Dynamic Systems, Measurement, and Control*, 128:36–43, 2006.
17. J. Lighthill. Flagellar hydrodynamics. *SIAM Review*, 18(2):161–230, 1976.
18. M. P. Kummer, J. J. Abbott, K. Vollmers, and B. J. Nelson. Measuring the magnetic and hydrodynamic properties of assembled-MEMS microrobots. In *Proc. IEEE Int. Conf. Robotics and Automation*, pages 1122–1127, 2007.
19. D. J. Bell, L. X. Dong, B. J. Nelson, M. Golling, L. Zhang, and D. Grützmacher. Fabrication and characterization of three-dimensional of InGaAs/GaAs nanosprings. *Nano Letters*, 6:725–729, 2006.